crystals

MDPI

Article

A Concept Crystal Habit Phase Diagram and Data for Curcumin in Isopropanol: Classical Versus Non-Classical Crystallization

Mahmoud Ranjbar [1], Mayank Vashishtha [1], Gavin Walker [1] and K. Vasanth Kumar [1,2,*]

[1] Synthesis and Solid-State Pharmaceutical Centre, Department of Chemical Sciences, Bernal Research Institute, University of Limerick, V94 T9PX Limerick, Ireland; gavin.walker@ul.ie (G.W.)
[2] Chemical and Process Engineering, Faculty of Engineering and Physical Sciences, University of Surrey, Guildford GU2 7XH, UK
* Correspondence: v.kannuchamy@surrey.ac.uk

Abstract: Cooling crystallization experiments of curcumin in isopropanol confirmed that curcumin can crystallize via classical or nonclassical pathways, depending on the levels of supersaturation and supercooling. Light microscopy analysis revealed that classical crystallization produces needle-shaped single crystals with an equilibrium habit, while nonclassical crystallization results in spherulitic mesocrystals. Through a series of experiments under various conditions, we developed a crystal habit phase diagram for curcumin in pure isopropanol. Presented here for the first time, this diagram illustrates the relationship between supersaturation, supercooling, and crystal habit, offering a valuable guide for controlling curcumin crystallization pathways.

Keywords: crystallization; nonclassical crystallization; mesocrystals; single crystals; crystal habit phase diagram; curcumin

1. Introduction

Crystallization is an important unit operation widely used in pharmaceutical industries for purifying active ingredients [1]. Classical crystallization is chemically controlled, where molecules in solution cluster and reorient into single crystals with an equilibrium crystal habit [2,3]. However, in one of our recent studies, we demonstrated that driving curcumin crystallization through nonclassical pathways can result in the formation of pristine surfaces that reject impurities, achieving a pure product in a single recrystallization step [4]. Unlike classical crystallization, nonclassical crystallization is controlled by entropy and involves mechanisms like two-dimensional nucleation and particle attachment, leading to mesocrystals with a preferred polymorph instead of single crystals. Our findings showed that these mesocrystals reject impurities, producing pure curcumin from crude material containing over 78% impurities in one step [4].

Mesocrystals, which are composed of nanocrystals, have significantly higher external surface area compared to single crystals, leading to faster dissolution [4–8]. Additionally, mesocrystals self-regulate their size, offering a narrow size distribution [4]. The recent advances in nonclassical crystallization have enabled the production of mesocrystals from organic, inorganic, and hybrid materials like metal–organic frameworks [6,8–15]. However, the process of producing mesocrystals is still challenging, as it requires extensive experimentation to identify the conditions that favor nonclassical crystallization. It is crucial to develop a guide that distills these experimental results into a single chart, helping to identify the conditions that lead to crystallization via classical, nonclassical, or hybrid pathways. In this work, we introduce the "crystal habit phase diagram (CHPD)" for curcumin

check for updates

Received: 23 December 2024
Revised: 13 March 2025
Accepted: 22 March 2025
Published: 25 March 2025

Citation: Ranjbar, M.; Vashishtha, M.; Walker, G.; Kumar, K.V. A Concept Crystal Habit Phase Diagram and Data for Curcumin in Isopropanol: Classical Versus Non-Classical Crystallization. *Crystals* **2025**, *15*, 296. https://doi.org/10.3390/cryst15040296

Copyright: © 2025 by the authors. Licensee MDPI, Basel, Switzerland. This article is an open access article distributed under the terms and conditions of the Creative Commons Attribution (CC BY) license (https://creativecommons.org/licenses/by/4.0/).

in isopropanol—a chart that maps key experimental conditions, such as supercooling and initial supersaturation, against the resulting crystal morphology. Curcumin, along with curcuminoids, demethoxycurcumin (DMC), and bisdemethoxycurcumin (BDMC) from turmeric, shows great potential in targeting cells for therapeutic purposes [16]. It interacts with multiple molecular pathways, aiding in the treatment of cancer, inflammation, neurodegenerative disorders, and other diseases like Alzheimer's, malaria, and HIV [16]. By binding to cell receptors and influencing signaling mechanisms, curcumin offers preventive and clinical efficacy against various inflammatory, proliferative, and angiogenic conditions [17–19]. Isopropyl alcohol (IPA) was used as the solvent based on the high-quality solubility data required for this study, obtained using process analytical technology tools in our lab [20–22]. Moreover, IPA is classified as a Class 3 solvent by regulatory authorities. The United States Food and Drug Administration (FDA) has approved isopropanol for use in drug formulations and active pharmaceutical ingredient (API) processing [23]. Its approval and low toxicity make it a suitable solvent for crystallization processes, including the development of curcumin-based products, as explored in this study.

There is currently significant interest in advancing the fundamental science of nonclassical crystallization as it even helps to understand the crystallization mechanism involved in biogenic and geological environments [24,25]. This endeavor necessitates a model system capable of crystallizing through both classical and nonclassical pathways. Such a system will enable experimental studies to uncover the mechanisms involved during the prenucleation stages and throughout nucleation. In this context, curcumin (CUR) was selected as the model compound for our proof-of-concept study, supported by findings from other research groups indicating that CUR can crystallize via either pathway [4,15]. Notably, these studies have shown that CUR often favors the nonclassical route, resulting in crystals that deviate from their equilibrium habit. Furthermore, CUR appears to be the first molecule observed experimentally to crystallize through both classical and nonclassical pathways in the same solvent without the need for any additives [4]. This unique characteristic makes CUR an ideal model system for enhancing our understanding of classical and nonclassical crystallization processes. To achieve this, it is crucial to identify the process conditions under which CUR crystallizes into mesocrystals via the nonclassical route or into needles via the classical pathway. Motivated by these scientific insights and based on our earlier proof-of-concept results, we conducted numerous cooling crystallization experiments, adjusting initial supersaturation, supercooling, and working temperatures to determine whether crystallization is entropically or chemically controlled. The findings were translated into a crystal habit phase diagram (CHPD), which provides a clear framework for developing procedures to manufacture curcumin mesocrystals. The CHPD delineates the operating conditions that favor either classical or nonclassical pathways and their corresponding crystal morphologies. This diagram can be utilized to design experiments aimed at studying the nucleation and prenucleation mechanisms involved in both classical and nonclassical crystallization processes.

2. Experimental Procedures

2.1. Materials

Crude CUR was purchased from Merck (CUR > 75% nominal purity). The solvent, HPLC-grade IPA (>99.9%), was purchased from Sigma-Aldrich and used without further purification. According to the HPLC analysis performed in our laboratory, the as-received curcumin contained 78.6 wt % CUR, 17.8 wt % DMC, and 3.6 wt % BDMC; the protocol used for the HPLC analysis is described elsewhere [22,26]. The CAS Registry Nos., suppliers, and the purity of the chemicals are given in Table 1.

Table 1. CAS Registry Number, purity of the chemicals used (as provided by the supplier and the analysis made in our laboratory using HPLC), and the molecular structure of the curcuminoids (last three rows in the table) involved.

Chemical	CAS Reg. No.	Suppliers	Purity
Curcumin	458-37-7	Sigma-Aldrich	Supplier specification: >75% CUR, with the remaining being DMC and BDMC. However, our analysis confirmed that it contains 78.6 wt % CUR, 17.8 wt % DMC, and 3.6 wt % BDMC [4].
Isopropanol	67-63-0	Sigma-Aldrich	>99.9%
Curcumin		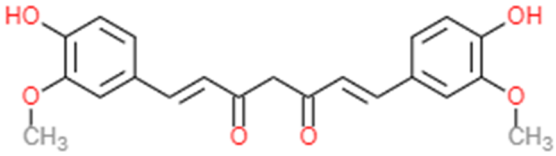	
Demethoxycurcumin		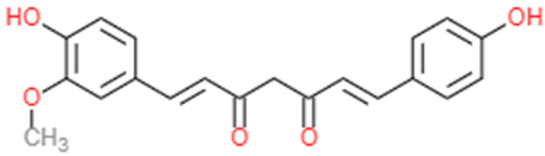	
Bisdemethoxycurcumin		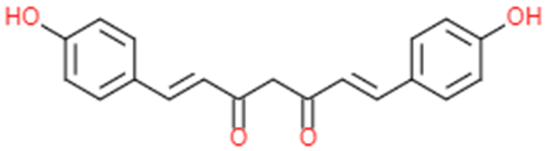	

2.2. Batch Cooling Crystallization Experiments

All the crystallization experiments were performed in batch mode in a 100 mL EasyMax synthesis workstation at the working temperature. We maintained a reactor volume of 100 mL for all the experiments. Agitation was provided using an overhead (with a pitched blade) stirrer. The temperature inside the crystallizer was maintained using an external jacket that relies on electrical heating and solid-state cooling technology. The agitation inside the crystallizer in all the experiments was maintained at 250 rpm. A known mass of crude curcumin is dissolved in isopropanol. Then, the solution is heated to a temperature, T^* + 10 °C, where T^* is the solubility temperature. The solution is then maintained at T^* + 10 °C for one hour to ensure complete dissolution of the curcumin in the solvent. Then, the solution is cooled back to the working temperature, T_w, at a cooling rate of 8 K/min. This should generate a supercooled solution of $\Delta T = T^* - T_w$. The solubility data required for this work was obtained using both gravimetric and process analytical technology tools in situ Raman and can be found elsewhere [20]. Briefly, the solubility of the curcumin versus the solubility temperature T^* follows the relationship: $c^* = 4 \times 10^{-5} T^{*3} - 0.0015\ T^{*2} + 0.0225 T^* + 0.2602$. For example, at 20 °C, the solubility of the pure CUR will be equal to 0.8 g/L. As the crude CUR contains 78.6 wt% of CUR, to create a solution of supersaturation, S = 4, it is essential to dissolve 3.2 × 100/78 = 4.10 g of CUR per 1000 mL of IPA or 0.041 g of CUR in 100 mL of IPA solvent. All the experiments were performed at least 4 to 5 times. The supersaturation was defined in terms of the ratio of the initial concentration of curcumin in the solution to the solubility concentration at T_w, $S = c/c^*$. In this work, we performed several experiments at different working temperatures and different degrees of supercooling. In all the crystallization experiments, we maintained the solution at the working temperature for ∼24 h to achieve complete saturation after

nucleation. The rapid cooling rate was chosen in all the experiments only to maintain the experimental consistency.

2.3. Microscopic Analysis

At the end of each crystallization experiment, we rapidly checked the particle morphology using an inverted light microscope (Model: Olympus IX53) integrated with an Olympus SC100 camera (Olympus, Tokyo, Japan) linked to a PC, enabling image capturing using the Olympus Stream Essentials software v2.3.

2.4. Powder X-Ray Diffraction (PXRD) Analysis

PXRD analysis of the spherulites and Form I curcumin was conducted using a PANalytical Empyrean diffractometer with Cu Kα1 radiation (λ = 1.5406 Å) at 40 kV and 35 mA over a 2θ range of 5–40°, with a step size of 0.1° and a total data collection time of 15 min. The crystallinity of the spherulites and Form I curcumin was confirmed by the presence of a flat baseline across the entire 2θ range of 5–40°. To calculate the size of crystallites using the size-only model, we used the Scherrer equation:

$$D = \frac{K\lambda}{\beta \cos\theta} \tag{1}$$

where D is the crystallite size (nm), K = Scherrer constant related to the shape factor of the particles (we used a value of 1), λ is the wavelength of the X-ray source (nm), β is the full width at half maximum (*FWHM*) of the selected diffraction peaks (in radians), and θ is the Bragg angle.

The Stokes–Wilson equation was used to estimate the microstrain from the peak broadening. This model assumes the lattice distortions cause variations in the d-spacing, which is reflected in the broadening of the diffraction peaks. This effect depends on the tangent of the diffraction angle:

$$\beta = 4\varepsilon \tan\theta \tag{2}$$

where ε is the microstrain.

The PXRD data was further analyzed using the Williamson–Hall (WH) plot with line profile analysis. The WH method assumes the peak broadening can be due to the combination of size and strain effects. The broadening of the peaks due to the size effects was captured from the Lorentzian integral breadth (or the FWHM), and the broadening due to the strain was captured using the Gaussian integral breadth. According to this method, the peak broadening is related to the size and the strain effects by the expression:

$$\beta \cos\theta = \frac{K\lambda}{D} + 4\varepsilon \sin\theta \tag{3}$$

From the plot of β cosθ versus 4ε sinθ, we calculated the crystallite size from the slope and the strain from the intercept using Equation (3).

3. Results and Discussion

In this study, we report the results obtained from the crystallization experiments at various working temperatures (T_w) and degrees of supercooling ($\Delta T = T - T_w$). Table 2 provides the process conditions, initial supersaturation, and final crystal morphology. Representative images of needle and spherulite crystals are shown in Figure 1. For better visualization, Figure 2 plots supersaturation ($S = c/c^*$) versus degree of supercooling and the corresponding crystal morphology. From these, we observed: (1) For curcumin in isopropanol, high supersaturation (3.66 to 6.62), high degree of supercooling (44.68 to 59.39 °C), and low working temperatures (3 to 10 °C) favor nonclassical crystallization,

producing spherulites (see Figure 1a–c). (2) If the degree of supercooling is below 34.39 °C, curcumin follows the classical crystallization pathway. Specifically, for the degree of supercooling between 34.39 and 43.01 °C, curcumin crystallizes following the classical crystallization route, regardless of supersaturation, highlighting the sensitivity of the crystallization pathway to the degree of supercooling. (3) We also identified a window where both spherulites and needles coexist. This occurs at T_w = 10 °C, ΔT = 43.41 °C with S = 3.43, or ΔT = 43.97 °C with S = 3.51 or 4.5. In summary, curcumin crystallizes via the nonclassical pathway when the degree of supercooling exceeds 44.68 °C and $S > 3.6$, and at working temperatures below 10 °C. These observations clearly indicate that, to drive curcumin molecules to crystallize via the nonclassical pathway, it is essential to establish specific working conditions, including a high degree of supercooling, high initial supersaturation, and a low working temperature.

Table 2. Experimental conditions that can be used as a guideline to produce curcumin single crystals and their mesocrystal versions. In the table, we show the solubility temperature that corresponds to the concentration of curcumin, c, which should provide the desired supersaturation at T_w. Also given is the solubility concentration at the working temperature.

T_w, °C	S	c*@ T_w	c, g/L	T*, °C	T* − T_w, °C	Morphology
3	6.62	0.76	5.03	62.39	59.39	Spherulites
3	6.2	0.76	4.71	60.95	57.95	Spherulites
3	4.8	0.76	3.65	54.92	51.92	Spherulites
3	3.6	0.76	2.74	47.68	44.68	Spherulites
5	4.77	0.77	3.67	55.09	50.09	Spherulites
5	4.25	0.77	3.27	52.22	47.22	Spherulites
5	4	0.77	3.08	50.68	45.68	Spherulites
10	4.77	0.78	3.72	55.41	45.41	Spherulites
3	3.2	0.76	2.43	44.74	41.74	Needles
3	3	0.76	2.28	43.17	40.17	Needles
5	3.6	0.77	2.77	48.01	43.01	Needles
5	3.2	0.77	2.46	45.06	40.06	Needles
5	3	0.77	2.31	43.49	38.49	Needles
10	4.25	0.78	3.32	52.54	42.54	Needles
10	4	0.78	3.12	51.01	41.01	Needles
10	3.6	0.78	2.81	48.34	38.34	Needles
10	3.2	0.78	2.50	45.38	35.38	Needles
15	4.77	0.8	3.82	56.02	41.02	Needles
15	4.25	0.8	3.40	53.18	38.18	Needles
20	4.77	0.84	4.01	57.20	37.20	Needles
20	4.25	0.84	3.57	54.39	34.39	Needles
10	4.5	0.78	3.51	53.97	43.97	Needles + Spherulites
10	4.4	0.78	3.43	53.41	43.41	Needles + Spherulites

Following the experimental protocols suggested by Kim et al., we characterized the presence of mesocrystal structures within the spherulites by analyzing the crystallite size and the potential existence of lattice distortions due to microstrain [9]. This was achieved by examining the peak broadening observed in the PXRD spectra of the spherulites. For comparison, we also characterized the PXRD spectra of needle-shaped Form I (FI) crystals. In Figure 3a, we present the powder X-ray diffractogram of the spherulites alongside that of Form I curcumin, which consists of needle-shaped single crystals. It is immediately evident that the PXRD pattern of the spherulites displays multiple broader peaks and several major peaks rather than a single dominant peak, which typically signifies preferential orientation along a specific crystallographic axis. The presence of multiple major peaks highlights the heterogeneous nature of spherulites and the absence of a strong preferential

orientation, in contrast to Form I curcumin, which exhibits a distinct preferential orientation towards the (2 0 2) plane [4]. As observed earlier, the spherulites exhibit a unique peak at $2\theta = 10.95°$ [4]. For clarity, Figure 3b presents the plot of FWHM versus 2θ for several major peaks in the diffractogram. Notably, peak broadening is consistently observed across all 2θ values, as indicated by the relatively smaller FWHM for needle-shaped crystals compared to spherulites. Additionally, Figure 3a reveals several shoulder peaks at $2\theta = 17.52°$, $2\theta = 22.88°$, and $2\theta = 23.53°$, along with peak shifts (e.g., $2\theta = 9°$ for spherulites vs. $2\theta = 8.95°$ for needles). These variations, in comparison to the single-crystal Form I, indicate strain differences in various crystallographic directions.

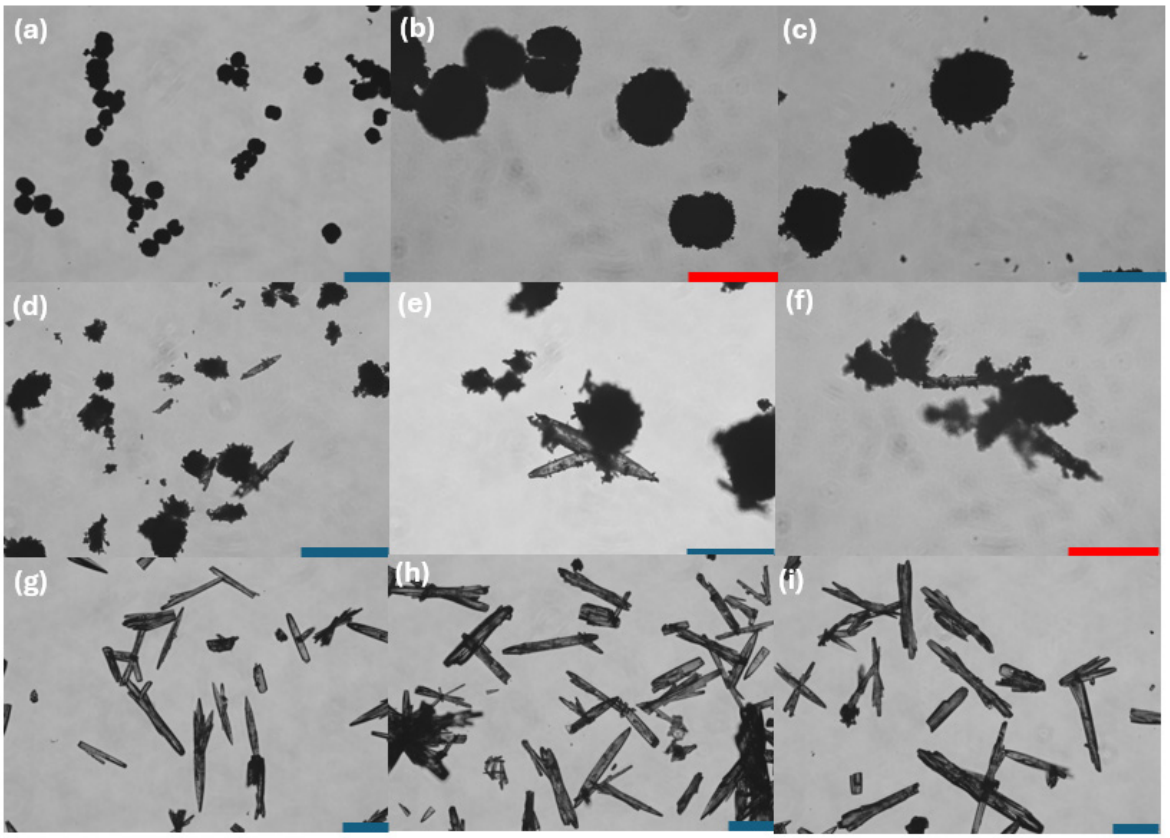

Figure 1. Optical microscope images of the spherulites, needles, and a batch that contains both spherulites and needles. These are only the representative images of the many crystals obtained from different batches. The process conditions of the batches that produced spherulites (**a**–**c**), spherulite plus needles (**d**–**f**), and needles (**g**–**i**) are given in Table 2 (scale bars are shown as blue line: 200 μm or as red line: 100 μm).

Conceptually, the broadening of peaks in PXRD patterns can be attributed to two main factors: crystallite size and microstrain. These two effects influence the peak width differently and can be analyzed using mathematical models such as the Scherrer equation and Williamson–Hall analysis [9]. When crystallites (or domains within the material) are very small, diffraction peaks become broader due to the limited number of planes contributing to the diffraction. Typically, the crystallite size can be obtained using the Scherrer equation, which assumes the peak broadening is only due to the crystallite size, given by: $\beta = K\lambda/L\cos\theta$. Where β is the full width at half maximum (FWHM) of the diffraction peak (in radians), K is the shape factor, λ is the X-ray wavelength, L is the crystallite size, and θ is the Bragg angle. Mathematically, according to the Scherrer expression, smaller crystallite size leads to broader peaks. On the other hand, microstrain that refers to lattice distortions (e.g., defects, dislocations, or internal stresses) can cause variations in the interplanar spac-

ing (*d*-spacing). These variations cause the diffraction peaks to broaden, and this effect depends on the tangent of the diffraction angle: $\beta = 4\varepsilon\tan\theta$, where ε is the microstrain. Mathematically, the microstrain increases with an increase in the diffraction angle (which is not the case for the broadening due to crystallite size). If the peak broadening is due to the microstrain, then it will be reflected in the form of peak broadening especially at a higher diffraction angle. A Williamson-Hall plot can separate the peak broadening due to crystallite size and microstrain.

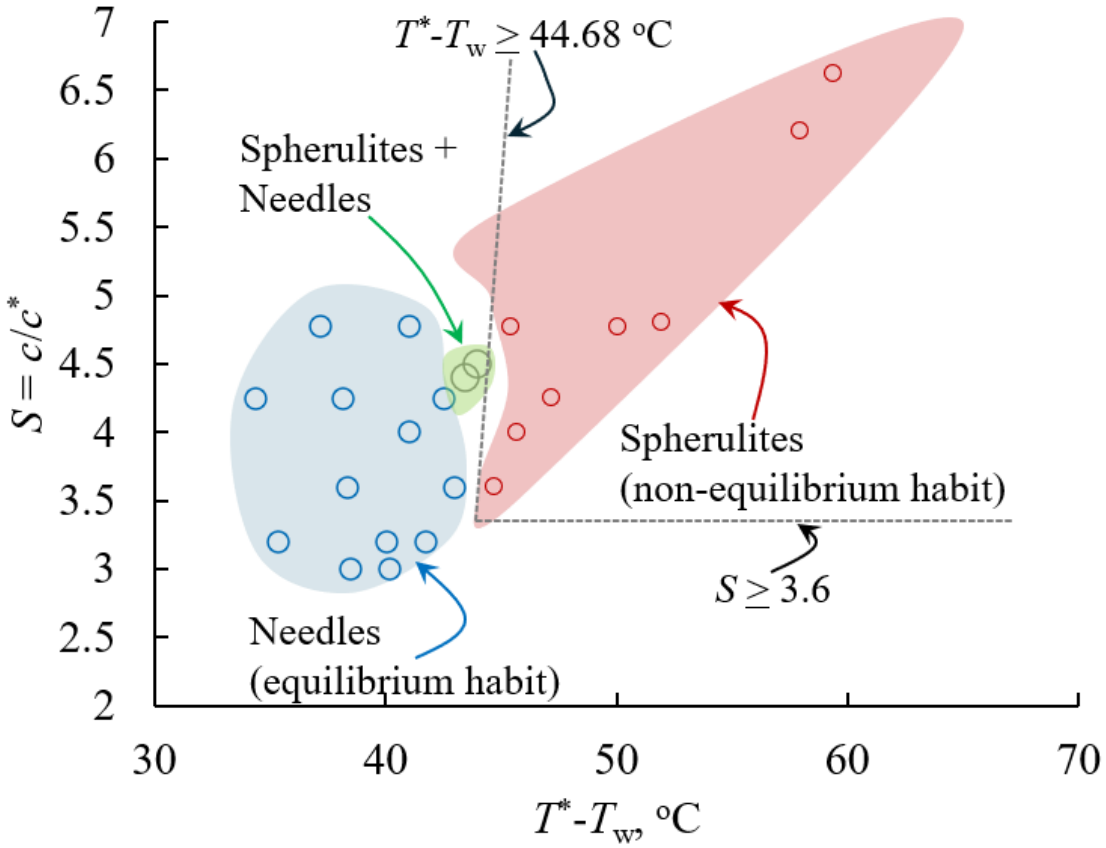

Figure 2. Plot of supersaturation versus the degree of supercooling for the crystallization of curcumin in isopropanol. Also shown are the experimental conditions where curcumin tends to crystallize following the classical and nonclassical crystallization pathways.

In Table 3, we present the calculated percentage strain and crystallite size derived from the strain-only model and the Scherrer method. In Table 3, we also present the stress and strain values obtained via the Williamson–Hall (WH) analysis for both the spherulites and a reference sample corresponding to single crystals with a needle-shaped habit. For the needle-shaped Form I crystals, the strain determined using the WH analysis was found to be equal to 0.39%, with a corresponding crystallite size of 106.6 nm. In contrast, for the spherulites, the strain was found to be 0.27%, while the crystallite size was significantly lower at 16.9 nm. This substantial reduction in crystallite size in the spherulites supports the hypothesis that they exhibit mesocrystalline characteristics rather than a conventional single-crystal structure. In the case of spherulites, a further analysis assuming peak broadening was solely due to size effects yielded a crystallite size of 22.5 nm, while considering only strain effects resulted in a strain value of 1.19%. Likewise, for the case of single crystals with needle habit when assuming peak broadening was solely due to strain effects, the crystallite size was calculated to be 83.3 nm with a strain of 0.43%. The crystallite size distribution obtained based on the size-only model clearly points to the fact that the needles contain a wide range of crystallites with a size distribution that spans

between 19 nm and 256 nm, with most of the crystallite size greater than 50 nm. For the case of spherulites, the crystallite size distribution clearly shows that these structures are composed of smaller-sized crystallites spanning between 16 and 50 nm. The larger crystallite size indicates both spherulites and needles retain long-range periodicity; however, the smaller size of the crystallites in the case of spherulites points towards the mesocrystal format of spherulites being composed of smaller-sized crystallites when compared to that of its single crystal versions. In terms of the strain in each crystal plane, the strain-only model overestimates the average microstrain, while the size-only model (i.e., the Scherrer equation) underestimates the average crystallite size when compared to that of the ones obtained from the Williamson–Hall plot. These discrepancies indicate that assuming strain or size alone as the sole contributor to peak broadening may not be entirely accurate. Instead, it is best to use the Williamson–Hall analysis to separate the contributions from crystallite size and microstrain accurately. The significantly reduced crystallite size in spherulites, along with their lower strain values compared to their single-crystal counterparts, suggests that the spherulites consist of aggregated nanocrystals with coherent interfaces rather than a continuous monolithic lattice. This structural distinction aligns with the expected characteristics of mesocrystals, where individual nanocrystallites exhibit a specific crystallographic alignment but remain distinct entities. The lower microstrain in the spherulites further suggests that these aggregates experience fewer internal stresses, potentially due to a more defect-tolerant assembly mechanism compared to conventional single crystals. These findings provide strong evidence supporting the mesocrystalline nature of the spherulites, distinguishing them from the conventional FI needle-shaped single crystals. Furthermore, the average crystallite size of spherulites seems to be almost ten times less than the average crystallite size of the FI curcumin. This essentially indicates that the Gibbs free energy, ΔG^*, required to form a stable crystallite in the case of spherulites must be smaller than the energy associated with the formation of stable crystallite during the formation of FI crystals. Based on the average crystallite size, the $\Delta G^*/KT$ value can be approximately scaled as $\ln(d/\Omega^{1/3})$, which corresponds to a value of 5.05 and 3.21 kJ/mol for FI and spherulites respectively [27]. This theoretical insight indicates that the energy barrier for spherulite formation is relatively lower than that of single crystals. In other words, spherulites develop in a solution with higher supersaturation compared to the conditions under which FI curcumin with an equilibrium habit forms.

Table 3. Crystallite size and average strain caused by lattice distortion.

Crystal Type	%Strain	Size	%Strain-Only	Size-Only
Spherulites (mesocrystals)	−0.31	15.23	0.73	158.13
Needles (FI)	0.39	106.65	0.43	83.39

To complement the results discussed based on the PXRD, in Figure 4 we show the scanning electron microscopic images of the curcumin spherulites and the FI needle-shaped crystals. It is evident that spherulites and needle-shaped crystals exhibit distinct morphologies. The SEM analysis of spherulites reveals key structural features: (i) a heterogeneous core at the center, and (ii) crystalline fibers of uniform length and width radiating outward to form primary spherical particles. These observations align with a three-stage growth process: (i) primary nuclei initially form amorphous-like spherical agglomerates, (ii) growth fronts emerge at the periphery, leading to the outgrowth of crystalline fibers, and (iii) the fibers continue to develop through a process known as growth-front nucleation. Unlike FI needle-shaped crystals, spherulites exhibit a hierarchical crystalline structure composed of filament-like structures originating from the core. The overall size of the spherulites

is approximately 80 microns, while the individual fibers are a few nanometers thick and extend 30–40 microns in length, maintaining a uniform radial orientation. In contrast, FI needle-shaped crystals exhibit an equilibrium crystal habit, where the crystallites grow with a well-defined crystallographic orientation. The structure of these crystals is relatively simple, with each crystal evolving in a uniform and predictable manner, consistent with classical crystallization mechanisms. The PXRD results confirm this structural distinction, as the larger crystallite size and lower lattice strain in FI needle-shaped crystals reflect their continuous, well-ordered lattice. These combined findings underscore the fundamental differences between the two forms. The smaller crystallite size and increased lattice strain in spherulites directly correlate with their mesocrystalline nature, where individual nanocrystallites are coherently assembled rather than forming a single, defect-free crystal.

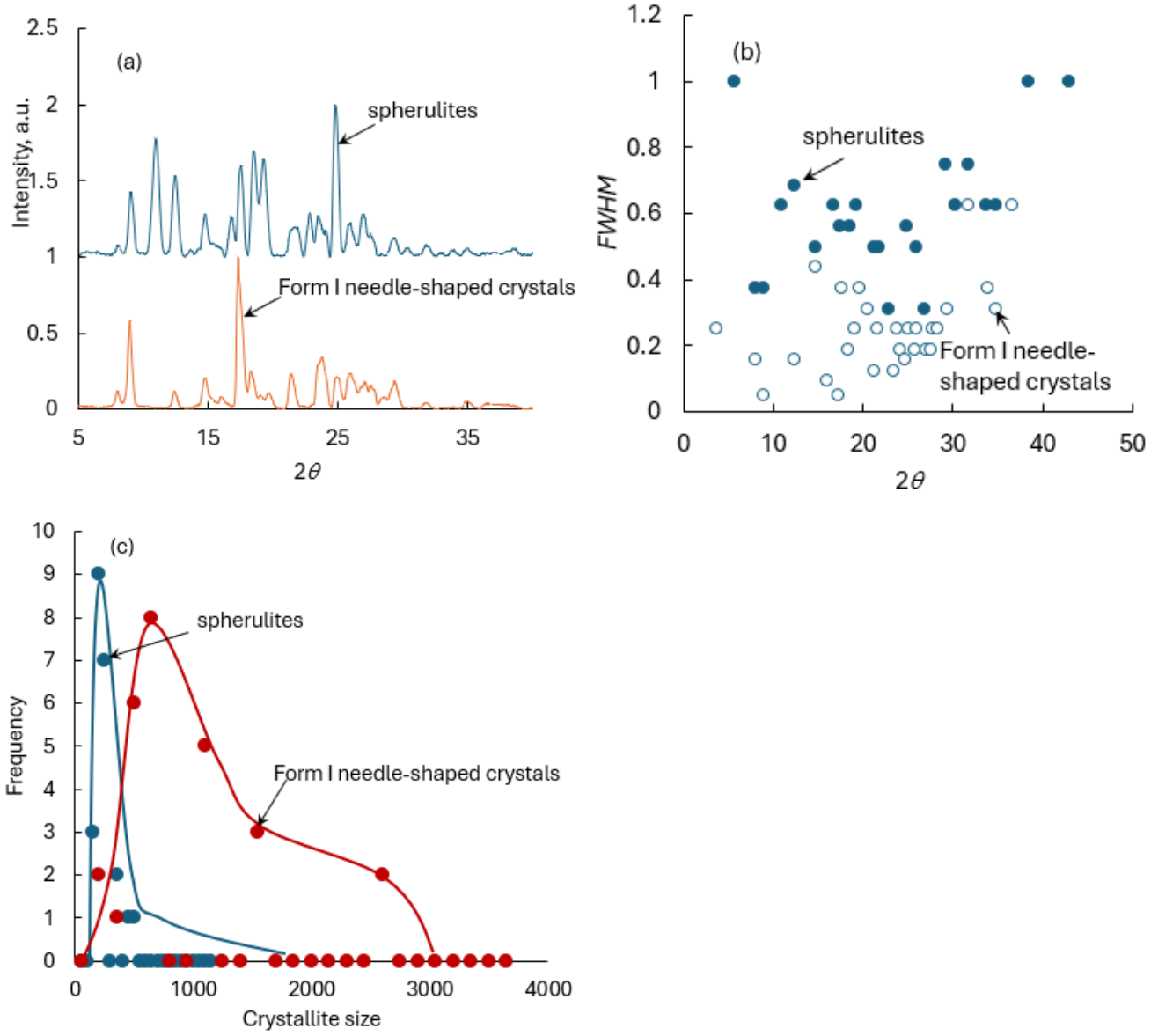

Figure 3. (**a**) PXRD of spherulites and the FI needle-shaped crystals obtained from the crude curcumin, (**b**) *FWHM* versus 2θ of the spherulites and the FI needle-shaped curcumin, and (**c**) distribution of the crystallite size obtained from the width of the major peaks assuming peak broadening is only due to the size effects.

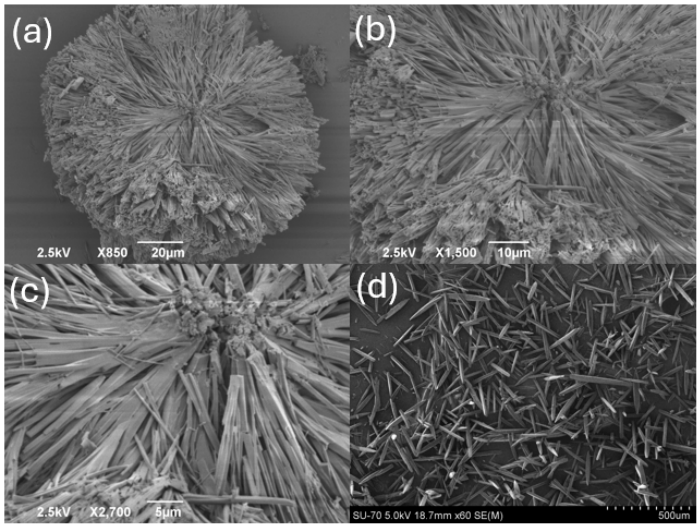

Figure 4. Scanning electron microscopic images of (**a**–**c**) spherulites at different magnifications, highlighting their structural details, and (**d**) FI needle-shaped crystals.

In our earlier work, we explained the selection of the crystallizing molecules to follow a classical or non-classical crystallization pathway from a kinetic standpoint. When there exists a combination of process conditions such as low working temperature, high degree of supercooling, and high supersaturation, then the process can be entropically controlled, which can drive the crystallizing molecules to follow a nonclassical pathway that includes growth via repeated two-dimensional nucleation, a perfectly or imperfectly oriented particle attachment mechanism that can produce spherulites or mesocrystals [4]. The term mesocrystal in this context refers to specific structural features of the spherulites. It describes a highly ordered assembly of nanocrystals aligned in a specific crystallographic orientation while remaining distinct entities, rather than merging into a single monolithic crystal. Unlike conventional single crystals, which typically evolve from a stable nucleus emerging from a prenucleation cluster, mesocrystals exhibit a hierarchical structure composed of nanoscale building blocks. This unique structural arrangement often results in distinctive properties, such as an increased surface area and modified mechanical behavior. This peculiar temperature effect on the morphology and the crystallization mechanisms has, however, never been reported for other crystallization systems; such observations were reported earlier to explain the molecular self-assembly process [3]. For cooling or isothermal crystallization systems, the strength of molecular interaction directionality (preference of a molecule to adsorb in a specific pattern driven by the forcefields involved) followed by the surface integration and condition at which this process is disturbed (due to the external factors such as higher supersaturation and degree of supercooling) can be taken as a line to observe the difference between chemical control and entropic control, respectively. If the process is less controlled by entropy, then crystallization can be considered to occur via ion-by-ion or molecule-by-molecule addition through Van der Waals and long-range interactions [3,28].

Alternatively, if the process is entropically controlled, then it is more likely that the molecule-by-molecule attachment process is disturbed, and the crystals grow via the formation of nanocrystallites at the expense of high supersaturation followed by oriented attachment of these nanocrystallites. The formation of spherulites in supercooled solution can be attributed to the existence (if any) of spatially dynamically heterogeneous molecules [28,29], a situation when some molecules move orders of magnitude faster than those situated only nanometers away. The ratio of rotational and translational diffusion coefficients decreases by orders of magnitude, and the molecules will translate increasingly

larger distances before they rotationally decorrelate from their initial orientation [30]. The dynamic heterogeneity can alter the shear viscosity and the translational and rotational diffusion coefficients. In crystallization, these diffusion coefficients characterize the rate of molecular translation and rotation that dictates the way molecules attach and align during the growth process [30,31]. In such a scenario, molecules in bulk solution become localized, and relaxation time increases by several orders of magnitude, and this will vitrify the crystallizing molecules at non-equilibrium conditions and possibly lead to mesocrystals with nonequilibrium habit. The existence of dynamic heterogeneity can be studied by in situ monitoring of the arrangement of prenucleation clusters and pre-crystallized units during the crystallization process and quantifications based on their mean square displacement [30], which is beyond the scope of this work; however, this issue will be exclusively studied and detailed in our future communications.

4. Conclusions

In conclusion, the plot of S versus $T^* - T_w$, referred to as the crystal habit phase diagram, serves as a useful guide for selecting process conditions that favor the formation of mesocrystals over single crystals with equilibrium habit. Nonclassical crystallization remains a relatively underexplored area, and researchers are still searching for systems that crystallize via both classical and nonclassical pathways. Curcumin, as highlighted in this study, is a key compound capable of crystallizing through either pathway, depending on the process conditions. This work presents the experimental conditions in the form of a crystal habit phase diagram, though further experiments at additional operating conditions could help better correlate process conditions with the final crystal morphology.

In this study, we presented the data obtained under limited process conditions, but these findings result from four years of extensive experimentation. For instance, in this study, all the experiments were conducted at a fixed cooling rate. Modifying the cooling rate can influence the nucleation rate by directly affecting the induction time, which in turn impacts the resulting crystal morphology. However, under the studied experimental conditions, the observed results and presented data remain valuable, particularly for the nonclassical crystallization research community. The crystal habit phase diagram and data offer valuable guidance for identifying the conditions necessary for both classical and nonclassical crystallization of curcumin in isopropanol. There is a critical need to study prenucleation and nucleation mechanisms in both pathways and curcumin—based on our results—is an ideal model compound for such studies. Additionally, these results hold importance for process industries, where needle-shaped crystals pose filtration challenges. We also present conditions where curcumin crystallizes into more easily filterable spherulites, addressing a key industrial issue.

Author Contributions: Conceptualization, K.V.K.; Methodology, M.R., M.V. and K.V.K.; Validation, M.V.; Formal analysis, M.R., M.V. and K.V.K.; Investigation, M.R. and M.V.; Resources, K.V.K.; Data curation, M.V.; Writing—original draft, M.R., M.V. and K.V.K.; Writing—review & editing, G.W. and K.V.K.; Supervision, G.W. and K.V.K.; Project administration, G.W.; Funding acquisition, G.W. and K.V.K. All authors have read and agreed to the published version of the manuscript.

Funding: We acknowledge the financial support of the Science Foundation Ireland (Grant 12/RC/2275, 12/RI/2345/SOF and 18/SIRG/5479). M.V. would like to acknowledge the Bernal Institute, Boston Scientific, Department of Chemical Sciences, and the University of Limerick Foundation for the funding support through the mULtiply program.

Data Availability Statement: The data is given within the manuscript.

Conflicts of Interest: The authors declare no conflict of interest.

References

1. Mullin, J.W. (Ed.) *Crystallization*, 4th ed.; Butterworth-Heinemann: Oxford, UK, 2001; ISBN 9780750648332.
2. Gebauer, D.; Kellermeier, M.; Gale, J.D.; Bergström, L.; Cölfen, H. Pre-Nucleation Clusters as Solute Precursors in Crystallization. *Chem. Soc. Rev.* **2014**, *43*, 2348–2371. [CrossRef]
3. Packwood, D.M.; Han, P.; Hitosugi, T. Chemical and Entropic Control on the Molecular Self-Assembly Process. *Nat. Commun.* **2017**, *8*, 14463. [CrossRef] [PubMed]
4. Kumar, K.V.; Ramisetty, K.A.; Devi, K.R.; Krishna, G.R.; Heffernan, C.; Stewart, A.A.; Guo, J.; Gadipelli, S.; Brett, D.J.L.; Favvas, E.P.; et al. Pure Curcumin Spherulites from Impure Solutions via Nonclassical Crystallization. *ACS Omega* **2021**, *37*, 23884–23900. [CrossRef] [PubMed]
5. Niederberger, M.; Cölfen, H. Oriented Attachment and Mesocrystals: Non-Classical Crystallization Mechanisms Based on Nanoparticle Assembly. *Phys. Chem. Chem. Phys.* **2006**, *8*, 3271–3287. [CrossRef] [PubMed]
6. Cölfen, H.; Antonietti, M. Mesocrystals: Inorganic Superstructures Made by Highly Parallel Crystallization and Controlled Alignment. *Angew. Chem. Int. Ed.* **2005**, *44*, 5576–5591. [CrossRef]
7. Sturm, E.V.; Cölfen, H. Mesocrystals: Structural and Morphogenetic Aspects. *Chem. Soc. Rev.* **2016**, *45*, 5821–5833. [CrossRef]
8. Wang, T.; Helmut Cölfen, A.; Antonietti, M. Nonclassical Crystallization: Mesocrystals and Morphology Change of $CaCO_3$ Crystals in the Presence of a Polyelectrolyte Additive. *J. Am. Chem. Soc.* **2005**, *127*, 3246–3247. [CrossRef]
9. Kim, Y.-Y.; Schenk, A.S.; Ihli, J.; Kulak, A.N.; Hetherington, N.B.J.; Tang, C.C.; Schmahl, W.W.; Griesshaber, E.; Hyett, G.; Meldrum, F.C. A Critical Analysis of Calcium Carbonate Mesocrystals. *Nat. Commun.* **2014**, *5*, 4341. [CrossRef]
10. Wang, H.; Xin, L.; Wang, H.; Yu, X.; Liu, Y.; Zhou, X.; Li, B. Aggregation-Induced Growth of Hexagonal ZnO Hierarchical Mesocrystals with Interior Space: Nonaqueous Synthesis, Growth Mechanism, and Optical Properties. *RSC Adv.* **2013**, *3*, 6538–6544. [CrossRef]
11. Lenders, J.J.M.; Dey, A.; Bomans, P.H.H.; Spielmann, J.; Hendrix, M.M.R.M.; de With, G.; Meldrum, F.C.; Harder, S.; Sommerdijk, N.A.J.M. High-Magnesian Calcite Mesocrystals: A Coordination Chemistry Approach. *J. Am. Chem. Soc.* **2012**, *134*, 1367–1373. [CrossRef]
12. Yang, L.; Killian, C.E.; Kunz, M.; Tamura, N.; Gilbert, P.U.P.A. Biomineral Nanoparticles Are Space-Filling. *Nanoscale* **2011**, *3*, 603–609. [CrossRef] [PubMed]
13. Xia, D.; Ouyang, M.; Wu, J.X.; Jiang, Y.; Piao, H.; Sun, S.; Zheng, L.; Rantanen, J.; Cui, F.; Yang, M. Polymer-Mediated Anti-Solvent Crystallization of Nitrendipine: Monodispersed Spherical Crystals and Growth Mechanism. *Pharm. Res.* **2012**, *29*, 158–169. [CrossRef] [PubMed]
14. Wohlrab, S.; Pinna, N.; Antonietti, M.; Cölfen, H. Polymer-Induced Alignment of DL-Alanine Nanocrystals to Crystalline Mesostructures. *Chem. Eur. J.* **2005**, *11*, 2903–2913. [CrossRef] [PubMed]
15. Thorat, A.A.; Dalvi, S.V. Particle Formation Pathways and Polymorphism of Curcumin Induced by Ultrasound and Additives during Liquid Antisolvent Precipitation. *CrystEngComm* **2014**, *16*, 11102–11114. [CrossRef]
16. Sanphui, P.; Bolla, G. Curcumin, a Biological Wonder Molecule: A Crystal Engineering Point of View. *Cryst. Growth Des.* **2018**, *18*, 5690–5711.
17. Salehi, B.; Stojanović-Radić, Z.; Matejić, J.; Sharifi-Rad, M.; Anil Kumar, N.V.; Martins, N.; Sharifi-Rad, J. The Therapeutic Potential of Curcumin: A Review of Clinical Trials. *Eur. J. Med. Chem.* **2019**, *163*, 527–545. [CrossRef]
18. Radha, R.; Paul, V.; Anjum, S.; Bouakaz, A.; Pitt, W.G.; Husseini, G.A. Enhancing Curcumin's Therapeutic Potential in Cancer Treatment through Ultrasound Mediated Liposomal Delivery. *Sci. Rep.* **2024**, *14*, 10499. [CrossRef]
19. Fuloria, S.; Mehta, J.; Chandel, A.; Sekar, M.; Rani, N.N.I.M.; Begum, M.Y.; Subramaniyan, V.; Chidambaram, K.; Thangavelu, L.; Nordin, R.; et al. A Comprehensive Review on the Therapeutic Potential of *Curcuma Longa* Linn. in Relation to Its Major Active Constituent Curcumin. *Front. Pharmacol.* **2022**, *13*, 820806. [CrossRef]
20. Ranjbar, M.; Vashishtha, M.; Gadipelli, S.; Ramisetty, K.; Walker, G.; Brett, D.J.L.; Kumar, K.V. Pseudo Second Order Kinetic Expression to Predict the Kinetics of the Anomalous Crystal Growth of Curcumin in Impure Solution. *Cryst. Eng. Comm.* **2024**, *26*, 1077–1089. [CrossRef]
21. Heffernan, C.; Ukrainczyk, M.; Zeglinski, J.; Hodnett, B.K.; Rasmuson, Å.C. Influence of Structurally Related Impurities on the Crystal Nucleation of Curcumin. *Cryst. Growth Des.* **2018**, *18*, 4715–4723. [CrossRef]
22. Heffernan, C.; Ukrainczyk, M.; Gamidi, R.K.; Hodnett, B.K.; Rasmuson, Å.C. Extraction and Purification of Curcuminoids from Crude Curcumin by a Combination of Crystallization and Chromatography. *Org. Process Res. Dev.* **2017**, *21*, 821–826. [CrossRef]
23. FDA. Innovation and Continuous Improvement in Pharmaceutical Manufacturing Pharmaceutical CGMPs for the 21st Century. Available online: https://www.fda.gov/media/77391/download (accessed on 13 March 2025).
24. Russo, J.; Tanaka, H. Nonclassical Pathways of Crystallization in Colloidal Systems. *MRS Bull.* **2016**, *41*, 369–373. [CrossRef]
25. De Yoreo, J.J.; Gilbert, P.U.P.A.; Sommerdijk, N.A.J.M.; Penn, R.L.; Whitelam, S.; Joester, D.; Zhang, H.; Rimer, J.D.; Navrotsky, A.; Banfield, J.F.; et al. CRYSTAL GROWTH. Crystallization by Particle Attachment in Synthetic, Biogenic, and Geologic Environments. *Science* **2015**, *349*, aaa6760. [CrossRef] [PubMed]

26. Ukrainczyk, M.; Hodnett, B.K.; Rasmuson, Å.C. Process Parameters in the Purification of Curcumin by Cooling Crystallization. *Org. Process Res. Dev.* **2016**, *20*, 1593–1602. [CrossRef]
27. Auer, S.; Frenkel, D. Prediction of absolute crystal-nucleation rate in hard-sphere colloids. *Nature* **2001**, *409*, 1020–1023. [CrossRef]
28. Bennemann, C.; Donati, C.; Baschnagel, J.; Glotzer, S.C. Growing Range of Correlated Motion in a Polymer Melt on Cooling towards the Glass Transition. *Nature* **1999**, *399*, 246–249. [CrossRef]
29. Gránásy, L.; Pusztai, T.; Börzsönyi, T.; Warren, J.A.; Douglas, J.F. A General Mechanism of Polycrystalline Growth. *Nat. Mater.* **2004**, *3*, 645–650. [CrossRef]
30. Weeks, E.R.; Crocker, J.C.; Levitt, A.C.; Schofield, A.; Weitz, D.A. Three-Dimensional Direct Imaging of Structural Relaxation Near the Colloidal Glass Transition. *Science* **2000**, *287*, 627–631. [CrossRef]
31. Gasser, U.; Weeks, E.R.; Schofield, A.; Pusey, P.N.; Weitz, D.A. Real-Space Imaging of Nucleation and Growth in Colloidal Crystallization. *Science* **2001**, *292*, 258–262. [CrossRef]

Disclaimer/Publisher's Note: The statements, opinions and data contained in all publications are solely those of the individual author(s) and contributor(s) and not of MDPI and/or the editor(s). MDPI and/or the editor(s) disclaim responsibility for any injury to people or property resulting from any ideas, methods, instructions or products referred to in the content.